

# Flaring Activities of Fast Rotating Stars have Solar-like Latitudinal Distribution

Huiqin Yang<sup>1,2</sup>, Xin Cheng<sup>3</sup>, Jifeng Liu<sup>1,2,4</sup>, Shuai Liu<sup>1</sup>, Zhanhao Zhao<sup>3</sup>, Guiping Zhou<sup>1,4,5</sup>, Yijun Hou<sup>1,4,5</sup>, Changliang Gao<sup>1</sup>, and Zexi Niu<sup>1,4</sup>

<sup>1</sup> Key Laboratory of Optical Astronomy, National Astronomical Observatories, Chinese Academy of Sciences, Beijing 100101, China  
e-mail: yhq@nao.cas.cn

<sup>2</sup> Institute for Frontiers in Astronomy and Astrophysics, Beijing Normal University, Beijing 102206, China

<sup>3</sup> School of Astronomy and Space Science, Nanjing University, Nanjing 210093, China

<sup>4</sup> School of Astronomy and Space Sciences, University of Chinese Academy of Sciences, Beijing 100049, China

<sup>5</sup> State Key Laboratory of Solar Activity and Space Weather, Beijing 100190, China

January 29, 2025

## ABSTRACT

*Context.* The dynamo theory has always been one of the biggest mysteries in stellar physics. One key reason for its uncertainty is poor knowledge of the dynamo process on stars except the Sun. The most important observation feature of solar dynamo is that active regions only appear at low latitudes, which provides a crucial constraint to the dynamo theory, while Doppler imaging, the current technique to spatially resolve stellar hemisphere, is difficult to distinguish the equatorial region. Hence, the latitudinal distribution of active regions (LDAR) of stars is ambiguous and controversial, mainly due to the limit of the current technique for spatially resolving the stellar surface.

*Aims.* Fast rotating stars, which are young and active, are thought to operate with a different dynamo process than the Sun. We study their LDAR and compare them with the Sun to reveal the underlying dynamo process.

*Methods.* Flares are drastic and observational activity events, which occur in active regions. Here, we propose a new method to study how the apparent flaring activity varies with respect to the inclination to determine the LDAR of fast rotating stars.

*Results.* We find that the LDAR of fast rotating stars is consistent with that of the Sun, contrary to expectations. Our results provide a crucial constraint to stellar dynamo, indicating that the solar-like dynamo also applies to fast rotating stars, even spanning different stages of their evolution.

**Key words.** Stars:activity – Stars:flare – Sun:activity – Sun:flare

## 1. Introduction

One of the biggest mysteries in stellar physics is the dynamo theory, which explains how a star produces and sustains its magnetic fields(Charbonneau 2020; Hathaway 2015). Until now, the dynamo theory has been only well tested through observations of the Sun, which has been regarded as an extraordinary laboratory for stellar physics. Nevertheless, the Sun is only one particular sample, resulting in the fact that the constraints for dynamo theory are still very limited to date(Charbonneau 2020; Choudhuri 2017). Fortunately, this issue can be addressed by studying the dynamo process of stars and comparing them with the Sun, i.e. the solar–stellar connection method(Brun & Browning 2017). However, the biggest obstacle to investigating the dynamo process of other stars is that they are spatially unresolved, resulting in that the location information of the dynamo process is difficult to detect.

On the Sun, the most prominent feature of the dynamo process is that sunspots and active regions begin to appear at around 30° of latitude at the beginning of an activity cycle and propagate towards the equator as the activity cycle progresses (Char-

bonneau 2020; Hathaway 2015; Nandy & Choudhuri 2002). This feature presents the latitudinal distribution of active regions (LDAR) of the Sun and provides a crucial constraint to the solar dynamo. The technique of Doppler imaging, which is used to reconstruct images of stellar surface on other stars, is difficult to distinguish starspots near the equatorial region(Rice 2002; Berdyugina 2005; Piskunov et al. 1990; Roettenbacher et al. 2016). It could also be affected by stellar activities, resulting in spurious results (Berdyugina 2005; Strassmeier 2002; Bruls et al. 1998). This causes the LDAR of other stars to be ambiguous and controversial(Berdyugina 2005).

Flares are a kind of drastic energy release event on the Sun driven by magnetic reconnection(Hathaway 2015). Their locations can be used to locate where active regions appear. Assuming that flares on other stars originate from starspots, the locations of starspots can also be determined. The inclination (the angle of the stellar spin axis with respect to the observer’s line of sight.) determines what latitude range of a star can be observed and which latitude has the greatest contribution to the observation. By combining flares and inclinations of fast rotating

stars that have similar intrinsic activity levels, we propose that the information of LDAR for spatially unresolved stars can be revealed by the variation of the apparent flaring activity with the inclination.

## 2. Data and method

### 2.1. Sample selection

In this study, we combined the flaring activities of stars and their corresponding inclination to reveal the information of LDAR. It requires three observational quantities: flare, rotation and projected rotation velocity ( $v \sin i$ ), which are provided by the data of the *Kepler* mission and the Apache Point Observatory Galactic Evolution Experiment (APOGEE)-2 spectrograph ( $R \sim 22,000$ ) of Sloan Digital Sky Survey (SDSS).

We firstly selected common stars from the catalog of flaring stars (Yang & Liu 2019) and the catalog of rotation period (McQuillan et al. 2014) in the *Kepler* mission, which were  $\sim 2200$  stars. We then cross-match them with the catalog data from the APOGEE DR17 (Abdurro'uf et al. 2022). About 240 stars remained. To exclude poor-quality data, we removed  $\sim 20$  stars that have the following SDSS quality flags: (ASPCAPFLAGS): VSINI\_BAD, SN\_BAD, STAR\_BAD, CHI2\_BAD, VMICRO\_BAD; (STARFLAGS): BAD\_PIXELS, LOW\_SNR, VERY\_BRIGHT\_NEIGHBOR. We also removed  $\sim 20$  giants ( $\log g < 3.5$ ) whose spectrum broadening were dominated by macroturbulent velocity (Holtzman et al. 2018), and got the final sample of 201 stars.

The final sample includes 21 RS CVn binaries and 11 single-lined spectroscopic binaries identified by the non-single star and variability catalog of Gaia DR3 (Eyer et al. 2023). We also identified six double-lined spectroscopic binaries in our sample (SB2; see Section 2.4.1). Binaries are plotted in Figure 1 with triangles, but are not included in the further analysis.

### 2.2. Flaring activities of stars and the Sun

The *Kepler* mission has provided over 4-year continuous white-light curves of 0.2 million stars with unprecedented precision. About 3400 flaring stars produce 0.16 million flaring events (Yang & Liu 2019). For each star, the flaring activity  $R_{\text{flare}}$  is defined as the ratio of the total flare energy to total energy a star emitted during the observation (Yang et al. 2017):

$$R_{\text{flare}} = \frac{\sum E_{\text{flare}}}{\int L_{\text{bol}} dt} = \frac{\tilde{L}_{\text{flare}}}{L_{\text{bol}}}. \quad (1)$$

Here,  $\sum E_{\text{flare}}$  is the sum of all detectable flare energies during the whole observation;  $L_{\text{bol}}$  is the bolometric luminosity. The definition of  $R_{\text{flare}}$  is similar to the proxy of chromospheric activity  $R'_{\text{HK}}$  (Noyes et al. 1984) and coronal activity  $R_X$  (Wright et al. 2011) that is a normalized quantity that has removed the influence of stellar luminosity. The left panels of Figure 1 show an example of flaring stars with different activity levels, which can be visually distinguished from the frequency and size of flares.

The right panel of Figure 1 shows the rotation–activity relationship in terms of flaring activity, where the  $x$  axis is Rossby number ( $Ro$ ; the ratio of the rotation period to global convective turnover time) instead of rotation period. This canonical relationship has been validated by various activity proxies (Noyes et al. 1984; Wright et al. 2011; Yang & Liu 2019; Yang et al. 2017), which identifies two stages of stellar evolution: the saturated (faster, with higher activity) and unsaturated (slower, with

declining activity) regimes. In the saturated regime, the stellar activity of those fast rotating stars becomes saturated, so that they are thought to have the same intrinsic activity level.

However, given that the *Kepler* mission provides curves of the white-light band, the flaring location (Watanabe et al. 2013) and the limb darkening effect (Claret & Bloemen 2011) will be the main factor that influence the observed flare energy and number and in turn determine the apparent flaring activity. Figure 2 shows the solar surface on which  $\sim 38000$  solar flares from 1975 to 2017 are superimposed. We simulate observing the Sun as a star by the *Kepler* mission from equator-on (Figure 2a inclination  $i \approx 90^\circ$ ) to pole-on (Figure 2b  $i \approx 0^\circ$ ; see Section 2.5 for details of the simulation). The variation of inclination determines whether and where each flare is observed on the hemisphere. Thus, it results in a dramatic rise of the apparent flaring activity with an increase in inclination for the latitudinal distribution of solar flares (Figure 2c).

For comparison, we created three latitudinal distributions of solar flares by taking the equator as the axis of symmetry and increasing the latitude of flares by  $20^\circ$ ,  $40^\circ$ , and  $70^\circ$ , respectively (Figure 3). These three distributions correspond to the active regions in mid-latitude, high-latitude, and polar regions, respectively. Equally, we simulated observing them from different inclinations and obtain three distinct relationships between flaring activity and inclination (Figure 3).

#### 2.2.1. Flare detection and energy estimate

The flare detection is similar to previous studies (Yang et al. 2017, 2018; Yang & Liu 2019). We briefly summarize the method here. (1) A smoothing filter based on the spline algorithm was used to fit the quiescent flux or the baseline, where an iterative  $\sigma$ -clipping approach was applied to remove all outliers. (2) After detrending the baseline, several criteria were applied to sort out flare candidates, including the amplitude and duration (at least three continuous points higher than  $3\sigma$ ), the profile (the decay phase should be longer than the rise phase) and the check of false-positive signal (no break points within 3 hr, target pixel file check, neighboring star check). (3) All of the flares were manually checked especially for whose duration was comparable to the rotation period. We reconstructed the quiescent fluxes using the neighboring data points of rotation period. The left panels of Figure 1 show examples of flare detection.

We estimated the flare energy by assuming a flare radiated as a blackbody with an effective temperature of 9000 K per unit area (Kretzschmar 2011) and the flare area was estimated by the flare amplitude, the stellar radius, the stellar effective temperature, and the *Kepler* response function (Shibayama et al. 2013; Yang et al. 2017; Yang & Liu 2019). Its uncertainty is  $\sim 60\%$  (Shibayama et al. 2013).

#### 2.2.2. The flaring activity of the Sun

In order to quantify the flaring activity of the Sun ( $R_{\text{sun}}$ ), we firstly used the data of GOES soft X-ray (SXR) peak flux ( $F_{\text{SXR}}$ ) to estimate the bolometric flare energy ( $E_{\text{flare}}$ ). The comparison between  $F_{\text{SXR}}$  of SXR and  $E_{\text{flare}}$  (Kretzschmar 2011; Namekata et al. 2017) can derive an empirical relation:

$$\begin{aligned} \log(E_{\text{flare}}) &= a \cdot \log(F_{\text{SXR}}) + b \\ a &= 0.78_{-0.08}^{+0.08} \\ b &= 34.4_{-0.03}^{+0.03}. \end{aligned} \quad (2)$$

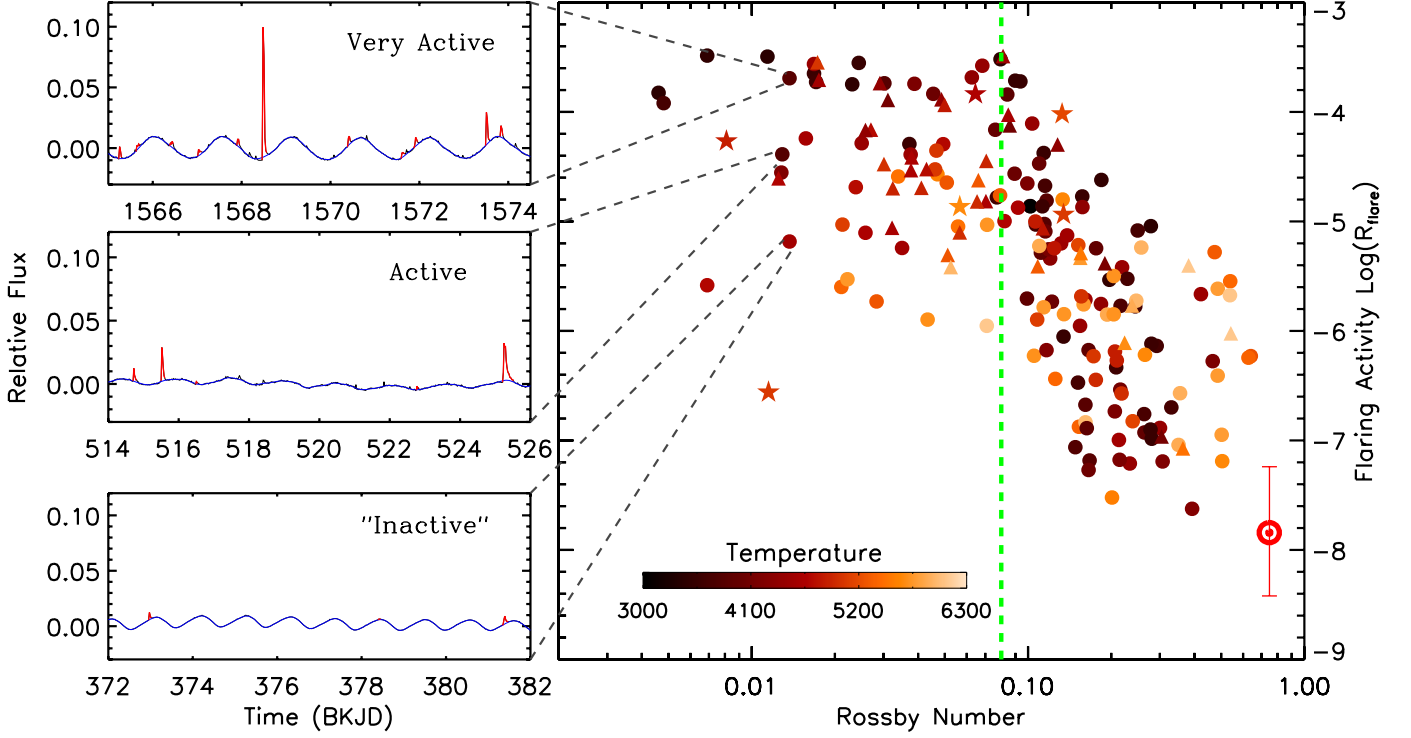


**Fig. 1.** Left panels: An example of flaring stars with different activity levels. Red curves denote flares. Blue curves are fitted baselines. Black curves are relative flux. Right panel: the rotation–flaring activity relationship. The  $x$  axis is Rossby number ( $Ro$ , the ratio of rotation period to the global convective turnover time), that has removed the influence of stellar mass. Circle: dwarf; triangle: binary; five-pointed star: subgiant. The green line ( $Ro = 0.08$ ) separates the saturated and unsaturated regimes. The Sun is marked with an  $\odot$  symbol.

The NOAA<sup>1</sup> has continuously recorded GOES SXR of  $\sim 77000$  solar flares from 1975 to 2017. We converted their  $F_{SXR}$  to  $E_{flare}$  and calculated the flare activity  $R_{flare}$  of the Sun (Equation 1) for each year (Figure 4). Figure 4 shows a 11-year cycle of solar flaring activity that is the same as sunspots and other activity proxies.

We then adopted the mean flaring activity of 33 years (three flaring cycles from 1976 to 2008) and the standard deviation as the flaring activity of the Sun and its uncertainty respectively. The location of the Sun is marked with an  $\odot$  symbol in Figure 1 and its value is

$$\log(R_{sun}) = -7.83^{+0.59}_{-0.59}. \quad (3)$$

### 2.3. Rossby number and the global convective turnover time

The Rossby number is the ratio of rotation period to convective turnover time. The convective turnover time cannot be observed directly and instead has to be estimated using either empirical fits (Noyes et al. 1984; Wright et al. 2011) or computations of theoretical models (Spada et al. 2017; Kim & Demarque 1996).

We used a grid of stellar evolutionary tracks from the Yale-Potsdam Stellar Isochrones (YaPSI) (Spada et al. 2017) to derive the global convective turnover time  $\tau_g$  by finding the best match of them to physical parameters of each star. Our method is similar to the previous study (Lehtinen et al. 2020). We firstly remapped the YaPSI tracks as a function of uniformly spaced “Equivalent Evolutionary Points” (EEPs) (Spada et al. 2017). We

then constructed a series of synthetic tracks by linearly interpolating EEPs with steps of  $0.02 M_{\odot}$ . We compared  $T_{eff}$  and  $\log g$  of each star with tracks from  $0.2 M_{\odot}$  to  $3 M_{\odot}$  and obtained  $\tau_g$  from the closest point of all the tracks to the star. In this way, we could repeat the above procedures to match  $\tau_g$  for different metallicities from  $-1.5$  to  $0.3$ . The final value of  $\tau_g$  was obtained by linear interpolation in metallicity.

The traditional rotation–activity relationship usually uses the local convective turnover time  $\tau_l$ , but  $\tau_g$  should be preferred with regard to this study because  $\tau_l$  is obtained by empirical fits (Noyes et al. 1984; Wright et al. 2011) that have hardly taken into account subgiants and giants. Our sample comprises subgiants which also conform to the rotation–activity relationship in terms of  $\tau_g$  (Lehtinen et al. 2020). The relation between  $\tau_l$  and  $\tau_g$  has been thoroughly discussed (Kim & Demarque 1996; Lehtinen et al. 2020; Spada et al. 2017; Landin et al. 2010; Mittag et al. 2018). In mathematics,  $\tau_g \approx 2.5\tau_l$  (Lehtinen et al. 2020; Mittag et al. 2018; Kim & Demarque 1996; Landin et al. 2010), which makes the critical Rossby number that separates the saturated and unsaturated regime to be  $\sim 0.1$ .

### 2.4. Inclination

The inclination of a star is the angle of the stellar spin axis with respect to the observer’s line of sight. Its sine value can be derived through the spectro-photometric method, which is governed by the following equation (Jackson & Jeffries 2010; Healy & McCullough 2020; Healy et al. 2023):

$$\sin i = \frac{v \sin i \cdot P}{2\pi R}. \quad (4)$$

<sup>1</sup> Available online: URL <https://www.ngdc.noaa.gov/stp/space-weather/solar-data/solar-features/solar-flares/x-rays/goes/xrs/>

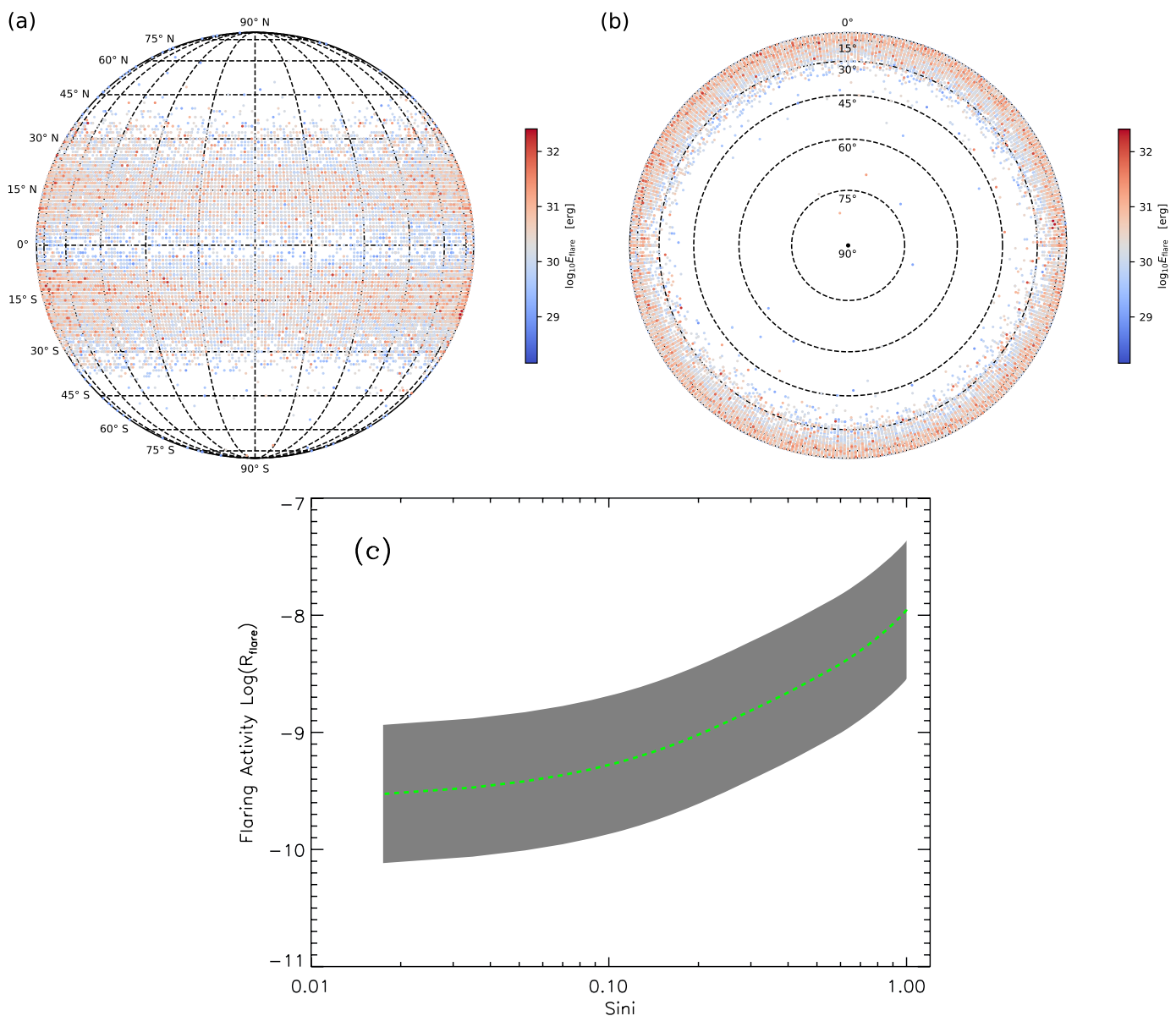


**Fig. 2.** Panel (a): About 38000 solar flares from 1975 to 2017 are superimposed on the solar hemisphere that is observed from edge-on. Panel (b): The same as (a) but observed from pole-on. Panel (c): The observed flaring activity of the Sun varies with the inclination. The shaded region represents the uncertainty caused by the maximum and minimum of the solar cycle.

Here,  $\text{vsini}$  is the projected rotational velocity measured from spectral broadening of high-resolution (Abdurro’uf et al. 2022),  $R$  is the stellar radius which can be estimated from the isochrone fitting (Somers et al. 2020), and  $P$  is the rotation period measured from lightcurve modulation (McQuillan et al. 2014).

#### 2.4.1. Projected rotation velocity

We measured the  $\text{vsini}$  of stars in our sample by spectra of APOGEE DR17 (Abdurro’uf et al. 2022), which had covered the Kepler field. We firstly generated theoretical templates through 1D LTE (local thermodynamic equilibrium) MARCS (Model Atmospheres with a Radiative and Convective Scheme) stellar atmosphere models. These templates were convolved with a Gaussian kernel ( $R \approx 13 \text{ km s}^{-1}$ ) to simulate instrumental broadening. We then convolved these non-rotating templates with varying profile of rotation to determine the best match of  $\text{vsini}$  to

the observation. In the matching process, we focused on five Fe I lines (15207.54, 15294.56, 15621.65, 15980.73, and 16486.69 Å) that exhibit minimal blending. The final result of  $\text{vsini}$  is the mean value calculated from these Fe I lines.

In order to validate our measurement, we compared them with values of  $\text{vsini}$  provided by the Apogee Stellar Parameter and Chemical Abundances Pipeline (ASPCAP). Our results generally show good agreement with ASPCAP’s findings, while there is a systematic offset of  $\sim 3 \text{ km s}^{-1}$  (Figure 5). We plot fitting lines of five stars whose difference of  $\text{vsini}$  between our measurement and ASPCAP is larger than  $5 \text{ km s}^{-1}$  (Figure A.1). Note that no matter which measurement is used, it will not change the results. During our measurement process, we found six SB2s which have seriously biased the measurements of ASPCAP (Figure A.2). We plotted them in Figure 1 with triangles, but did not include them in the further analysis.

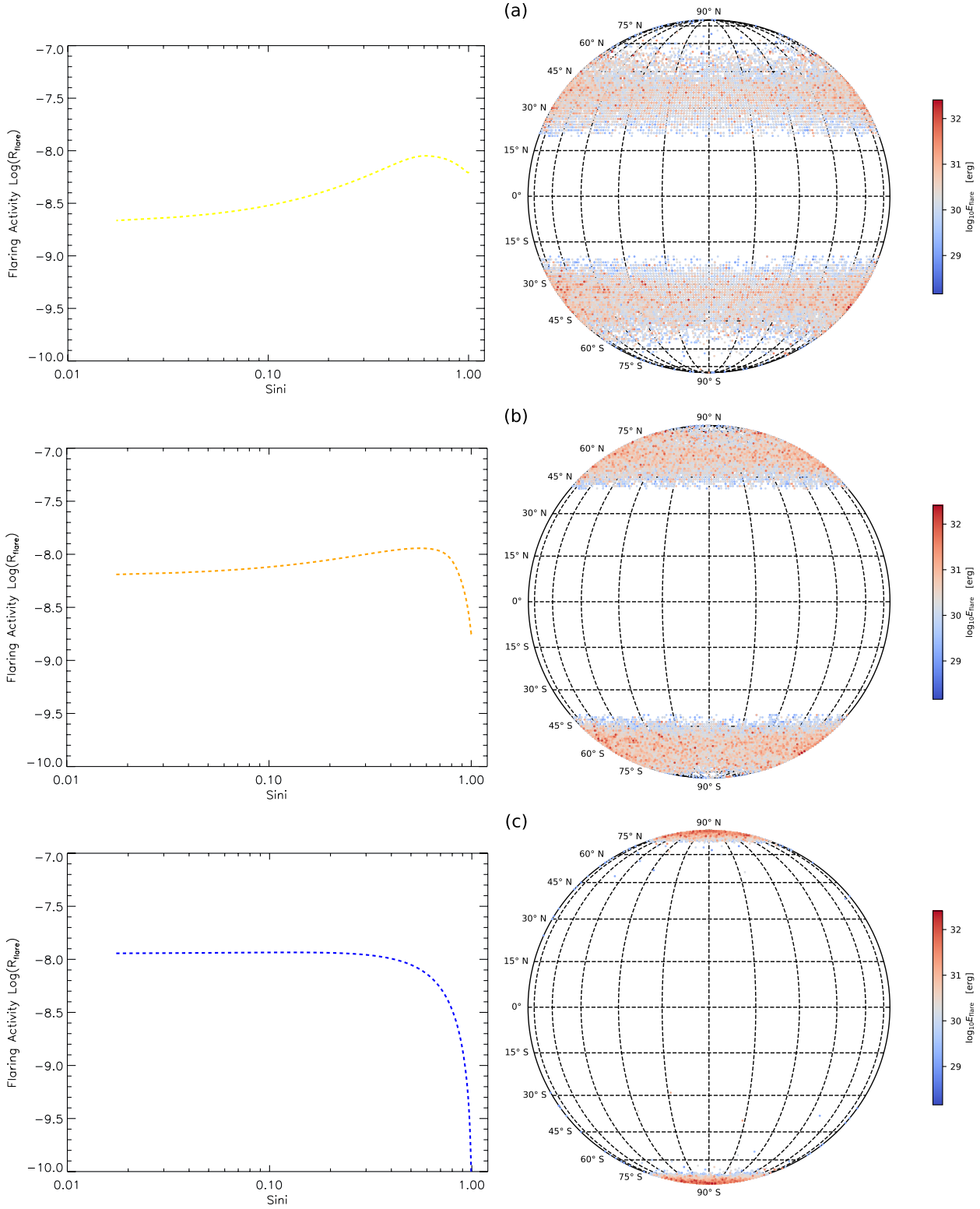


**Fig. 3.** The flaring activity vs. inclination for different LDAR. Right panels show the flaring region in mid latitude, high latitude and polar region, which are created by increasing the latitude of solar flares by  $20^\circ$ ,  $40^\circ$ , and  $70^\circ$ , respectively. Left panels show their corresponding relation for the flaring activity and inclination.

The mechanisms of spectroscopic broadening are mainly from rotation and macro-turbulence. The solar macro-turbulent velocity is  $\sim 3 \text{ km s}^{-1}$  and that of cooler stars is slightly smaller (Doyle et al. 2014). We therefore assumed the uncertainties of  $v \sin i$  to be  $3 \text{ km s}^{-1}$  or 10%, whichever was greater (Tayar

et al. 2015). Due to the resolution of APOGEE, the variance of its  $v \sin i$  rapidly increases below  $10 \text{ km s}^{-1}$  (Simonian et al. 2020). For stars of  $v \sin i < 10 \text{ km s}^{-1}$ , we used the measurements of ASPCAP and adopted a conservative policy by setting the lower error bar and upper error bar to be  $1 \text{ km s}^{-1}$  and

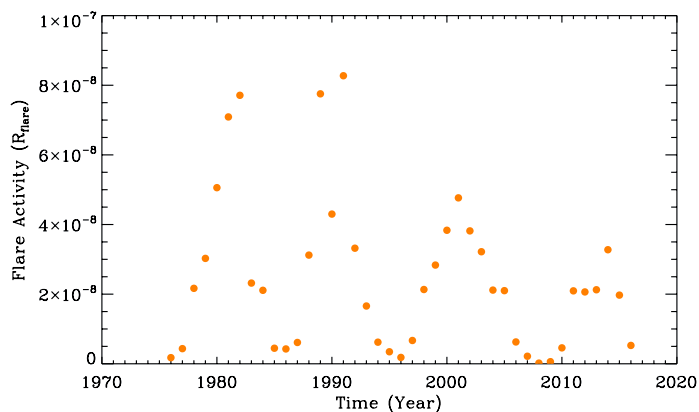


**Fig. 4.** The flaring activity of the Sun from 1975 to 2017. The solar flare energies are estimated based on the GOES soft X-ray data (Equation 2). The variation of the flaring activity shows a 11-year cycle.

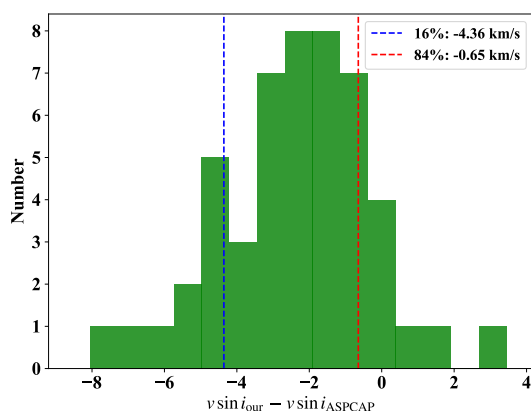


**Fig. 5.** A comparison of  $v \sin i$  between our measurements and that of ASPCAP for stars of  $v \sin i > 10 \text{ km s}^{-1}$ . The blue and red vertical dashed lines denote the 16th and 84th percentiles of the distribution respectively.

$10 \text{ km s}^{-1}$  respectively, although the detection limit of APOGEE is  $\sim 5 \text{ km s}^{-1}$  (Deshpande et al. 2013; Gilhool et al. 2018).

#### 2.4.2. Stellar radius

There is a widespread discrepancy between the radii of young, active stars and model predictions, which is the so-called radius inflation. This discrepancy is quite serious for fast rotating stars, which is up to 20% (Jackson & Jeffries 2014; Somers & Stassun 2017; Jaehnig et al. 2019). This is attributed to the fact that current stellar models have a simple treatment on the surface convection and do not account for the influence of magnetic activity on stellar parameters (Spada et al. 2013; Somers et al. 2020). For example, starspots inhibit convection, reducing the effective temperature of a star. The temperature cooling will result in a smaller radius in the isochrone fitting.

In order to estimate radii of our rapidly rotating, active stars, we used the Stellar Parameters of Tracks with Starspots (SPOTS) (Somers et al. 2020) to fit the effective temperature and log of the APOGEE parameters. The SPOTS models include the structural effect of starspots in solar-metallicity evolutionary tracks, ranging from spotless to a surface covering fraction ( $f_{\text{spot}}$ ) of 85%. It was found that in the saturation regime, the

covering fraction of spot is  $\sim 30\% - 40\%$  for G-type stars, and is  $\sim 40\% - 50\%$  for K- and M-type stars (Fang et al. 2016). Therefore, we adopted the SPOTS tracks of  $f_{\text{spot}} = 0.34$  for G-type stars ( $T_{\text{eff}} > 5000\text{K}$ ), and  $f_{\text{spot}} = 0.51$  for K- and M-type stars ( $T_{\text{eff}} < 5000\text{K}$ ). We also carried out the isochrone fitting through the traditional models of PARSEC (Chen et al. 2014) and YAPSI (Spada et al. 2017) and compared them with the SPOT-derived radii. We found that traditional models underestimated radii of rapid rotating stars, on average, by  $\sim 9\%$  for G-type stars and by  $\sim 11\%$  for K- and M-type stars. The comparison is consistent with previous studies on stars of open clusters (Somers & Stassun 2017; Jaehnig et al. 2019).

#### 2.4.3. Determination of inclination

Given that we determined  $\sin i$  through Equation 4 that involved a comparison of two correlated parameters: the calculated  $v$  and measured  $v \sin i$ , we thus performed Bayesian inference and determined the posterior probability distribution (PPD) of  $\sin i$  for each star (Masuda & Winn 2020).

We used the calculated  $v$ , measured  $v \sin i$  and their uncertainties to define the likelihood function of  $v$  and  $v \sin i$ , both of which are assumed to follow a Gaussian distribution. We set uniform priors for  $\sin i$  and  $v$  (Masuda & Winn 2020). We applied Bayes' theorem to set up an integral calculating  $p(\sin i | D)$  and directly computed the integral for the PPDs (Healy & McCullough 2020). For each distribution, we adopted the median value as the  $\sin i$ , with the 16th and 84th percentiles providing the uncertainties.

#### 2.4.4. Uncertainties of inclination

We summarize factors that may cause uncertainties in the parameters in Equation 4, which will result in an overestimate or underestimate of  $\sin i$ .

**Overestimate of  $\sin i$ :** (1) differential rotation will cause overestimate of rotation period  $P$ , if it is the solar-like differential rotation (i.e. the pole rotates slower than the equator). (2)  $v \sin i$  will be overestimated by turbulence and activity, which are serious for slowly rotators. (3)  $R$  is underestimated by stellar model especially for fast rotators (Radius inflation).

**Underestimate of  $\sin i$ :** (1) differential rotation will cause underestimate of rotation period  $P$ , if it is the anti-solar differential rotation (i.e. the pole rotates faster than the equator). (2) differential rotation will cause underestimate of  $v \sin i$  by a factor of  $\sim 5 - 10\%$  in solar-like rotators (Hirano et al. 2014).

We have dealt with the item (2) and (3) of overestimate in the above Sections by setting a proper uncertainty or taking account of the temperature cooling, while the item (1) of overestimate and the underestimate of  $\sin i$  are more complicated. Firstly, the study of asteroseismology on 40 solar-like stars shows that one-fourth of them have anti-solar differential rotation (Benomar et al. 2018), although the significance is not enough. Further analysis on their significance of signals and theoretical expectation suggest that fast rotators are dominated by solar-like differential rotation. We thus assume that stars of our sample are solar-like differential rotation (Gastine et al. 2014). The overestimated period and the underestimated  $v \sin i$  will act in opposite direction to change the determined inclination. Their effects will partially cancel out and cause a mean systematic underestimate of  $\sin i$  by 5.7% (Healy et al. 2023). We added this fractional error in quadrature to the upper error bar of our results.

## 2.5. Observe the Sun as a star through the telescope of the Kepler mission

We simulated observing the Sun through the Kepler mission from different inclinations. We should consider two factors that influence the observation of a flare. One is the visible fraction  $D$  of a latitude with respect to an inclination angle. It is governed by the following equation (Ilin et al. 2021):

$$D = \begin{cases} 1, & -\tan\theta \tan(\frac{\pi}{2} - i) < -1 \\ \frac{1}{\pi} \arccos(-\tan\theta \tan(\frac{\pi}{2} - i)), & -1 \leq -\tan\theta \tan(\frac{\pi}{2} - i) \leq 1 \\ 0, & -\tan\theta \tan(\frac{\pi}{2} - i) > 1 \end{cases} \quad (5)$$

Here, the inclination angle is  $i$  and the latitude is  $\theta$ . This equation determines the probability that a flare is observed at a given latitude and inclination. We take it as the observed fraction of the flare energy at the latitude.

Another factor is the limb-darkening effect in the Kepler band (Claret & Bloemen 2011). We adopted the quadratic function of the limb-darkening law:

$$\frac{I(\mu)}{I(1)} = 1 - a(1 - \mu) - b(1 - \mu)^2 \quad (6)$$

$$\begin{aligned} \mu &= \cos(\phi) \\ a &= 0.40 \\ b &= 0.26 \end{aligned}$$

Here,  $I$  is the observed intensity,  $\phi$  is the angle between the line of sight and the normal to a given point of the stellar surface. The parameters  $a$  and  $b$  are the limb-darkening coefficients obtained under the condition that  $T_{\text{eff}} = 5750\text{K}$ ,  $\log g = 4.5$ ,  $[\text{M}/\text{H}] = 0$ , and micro-turbulent velocity is  $2 \text{ km s}^{-1}$  (Claret & Bloemen 2011). Note that the influence of magnetic activity on the limb-darkening coefficients is less than 5% (Kostogryz et al. 2024), which is negligible in this study.

We compared the flare flux intensity  $F$  and the flare duration  $\tau$  by the solar and stellar flares (Namekata et al. 2017; Maehara et al. 2015) and obtained  $\tau \sim F^{2.73}$ . Given that the relation between the flare energy  $E$  and the flare duration was  $E \sim \tau^3$  (Namekata et al. 2017; Maehara et al. 2015), we got  $E \sim F^{8.19}$ .

Based on above relations, we got the relation between the observed flare energy  $E_{\text{observed}}$  and the intrinsic flare energy  $E$ :

$$E_{\text{observed}} = E \cdot D \cdot (1 - a(1 - \mu) - b(1 - \mu)^2)^{8.19} \quad (7)$$

By virtue of Equation 7, we calculated the apparent flaring activity with decreasing inclination from equator-on to pole-on, which are shown in Figure 2c.

We increased the latitude of solar flares by  $20^\circ$ ,  $40^\circ$ , and  $70^\circ$  respectively, to simulate LDAR in mid-latitude, high-latitude and polar regions (Figure 3) and obtained three distinct relationships between the flaring activity and inclination.

## 3. Result and discussion

### 3.1. The comparison between the Sun and stars on the latitudinal distributions of flaring activities

We derive the inclinations of flaring stars in Figure 1 through three observational quantities including the projected rotational

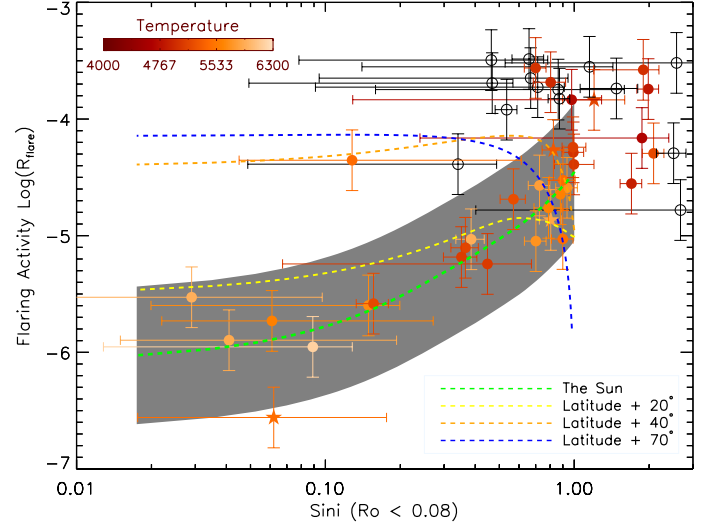


**Fig. 6.** The relation between the flaring activity and the inclination in the saturated regime ( $Ro < 0.08$ ). Circles are dwarfs and five-pointed stars are subgiants. Open circles represent M-type stars. The green line denotes the variation of the solar flaring with the inclination and the shaded region represents the uncertainty caused by the maximum and minimum of the solar cycle. The other three dashed lines denote the variation caused by the mock data, which correspond to the flaring region distributing at mid latitude ( $+20^\circ$ ), high latitude ( $+40^\circ$ ) and polar region ( $+70^\circ$ ) respectively. All the dashed lines have been shifted vertically for a comparison.

velocity ( $v \sin i$ ) (Abdurro'uf et al. 2022), rotation period (McQuillan et al. 2014) and stellar radius (Somers et al. 2020). The values of  $\sin i$  greater than 1 are nearly equator-on stars or probably unresolved binaries (Healy et al. 2023; Simonian et al. 2020). We compare the inclination  $\sin i$  and the apparent flaring activity in the saturated regime (Figure 6) and unsaturated regime (Figure 7).

In the saturated regime, the magnetic field strength of fast rotating stars becomes saturated (Reiners et al. 2009). Thus their intrinsic activities are believed to be independent of rotation and should have the same activity level (Noyes et al. 1984; Wright et al. 2011; Yang et al. 2017). However, the variation of the apparent flaring activities we derived is found to be related to the inclination (Figure 6). This most likely results from the LDAR of those fast rotating stars. The comparison between the stellar and solar variations with different latitude distribution of flares (dashed lines of Figure 6) shows that, for F-, G- and K-type stars ( $4000 \text{ K} < T_{\text{eff}} < 6300 \text{ K}$ ) with a fast rotation, their LDAR is of solar-like. For M-type stars ( $T_{\text{eff}} < 4000 \text{ K}$ ), although they have a higher activity level, we do not have sufficient observations to identify their relationship with the inclination.

In the unsaturated regime, we divide Rossby number into three intervals to reduce the influence of rotation (Figure 7). In each interval, we assume that stars have the same intrinsic flaring activity and check if they conform to the solar relation. The uncertainty of  $v \sin i$  increases rapidly as stars slow down and it is even impossible to detect flaring stars with low inclination because of the exponential decay of the apparent flaring activity along with decreasing inclination. In spite of that, we can still find a trend (or a positive correlation) between the apparent flaring activity and inclination, especially for relatively fast rotators ( $0.08 < Ro < 0.15$  the top left panel). As the rotation decreases, this trend becomes more and more ambiguous because of the observation limit. Given that stars in the unsaturated regime are sup-

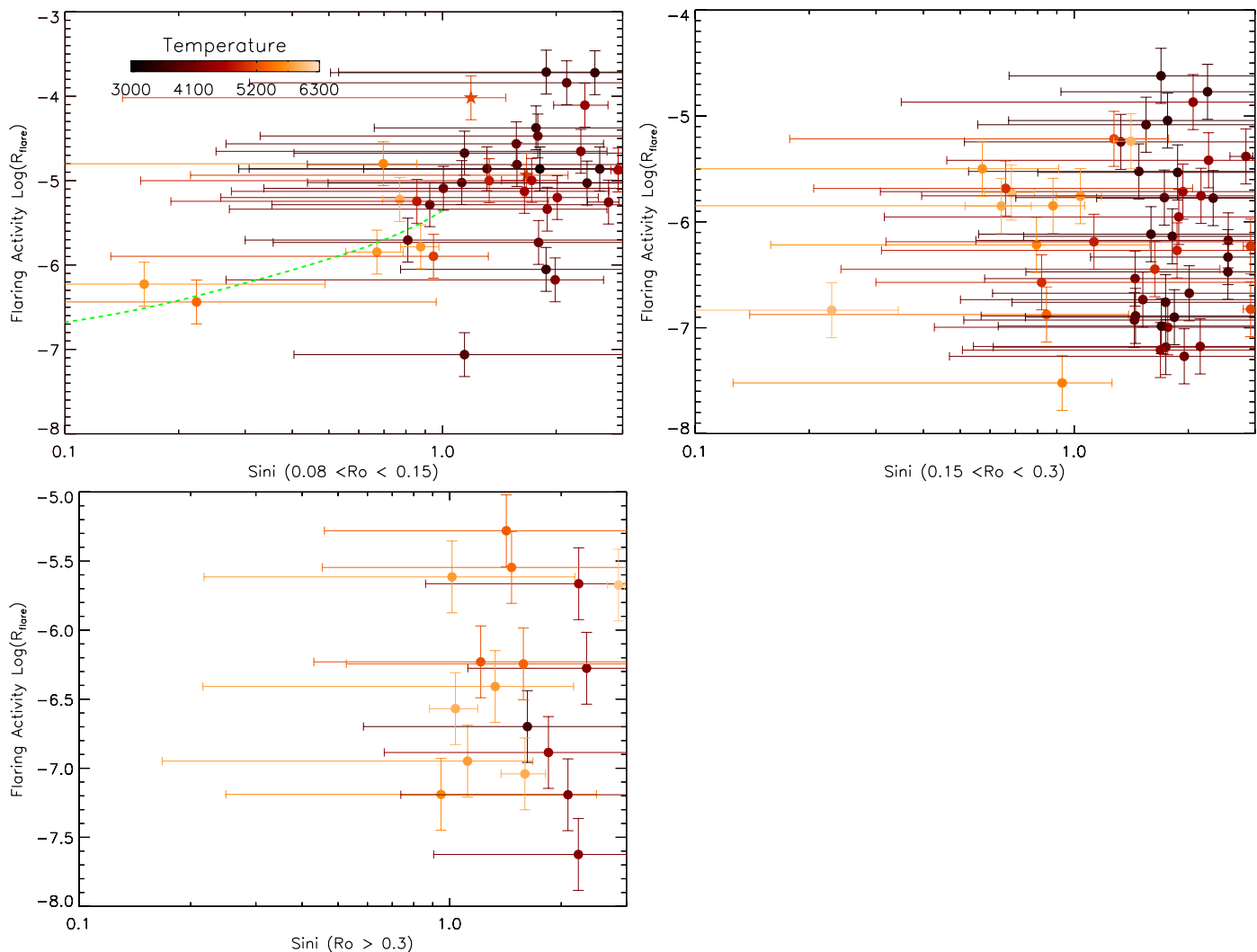


**Fig. 7.** The flaring activity vs. inclination for stars in the unsaturated regime. In order to reduce the influence of rotation, the Rossby number was divided into three intervals. The large uncertainty is due to the decline of  $v\sin i$  with decreasing rotation and our conservative policy for star of  $v\sin i < 10 \text{ km s}^{-1}$  (the upper limit and lower limit of them were set to be  $1 \text{ km s}^{-1}$  and  $10 \text{ km s}^{-1}$  respectively).

posed to be solar-like dynamo, they are more likely to have the same relation as the Sun. We suggest that better observations may validate this trend in the future.

### 3.2. Interpretation of the LDAR of fast rotating stars

On the Sun, very few flares were found outside of active regions (Hathaway 2015). The latitudinal distribution of flares can represent the LDAR. The similarity of flaring latitudes demonstrates that the LDAR of fast rotating stars is highly similar to that of the Sun (Figure 6).

Various tests have shown that Doppler imaging is inefficient for the equatorial region where spots are recovered with reduced area and contrast (Berdyugina 2005; Rice 2002). Our results find a crucial evidence for flares being mainly distributed at latitudes of  $\theta \leq 30^\circ$ . Moreover, our sample includes about 50 stars with over 4 years of observations. Since a faster rotator has a shorter stellar cycle (Boro Saikia et al. 2018), the four-year observations may cover the whole stellar cycle of those stars. If their starspots propagate poleward, the corresponding initial emergence latitudes should be at latitudes of  $\theta \leq 10^\circ$  to ensure that they are always at low latitudes of  $\theta \leq 30^\circ$  through a whole stellar cycle.

On the other hand, since fast rotating stars tend to form initial starspots at higher latitudes of  $\theta \geq 30^\circ$  where the latitudinal differential rotation is stronger and the toroidal field generation is more efficient (Işık et al. 2018; Zhang et al. 2024), we suggest that starspots of fast rotating stars begin to appear at around  $30^\circ$  of latitude and propagate equatorward, highly resembling with that of the Sun.

Another interesting and still controversial feature in stellar Doppler images are large polar spots or cool active regions over the stellar poles, which are the so-called polar cap (Strassmeier 2002; Berdyugina 2005). This feature is explained by the scenario that faster rotators give rise to higher latitude of active region (Strassmeier 2002; Berdyugina 2005). Our results do not support the scenario of polar cap for F-, G-, and K-type stars because it will result in a totally different relation between the flaring activity and inclination (the blue dashed line in Figure 6).

Admittedly, the prevailing viewpoint based on the Doppler imaging and simulations believes that polar spots were widespread (e.g., Schuessler & Solanki 1992; Choudhuri & Gilman 1987; Strassmeier 2002), which contradict our results. We should note that the polar cap could be artifacts caused by stellar activity (Bruls et al. 1998), microturbulence and blend

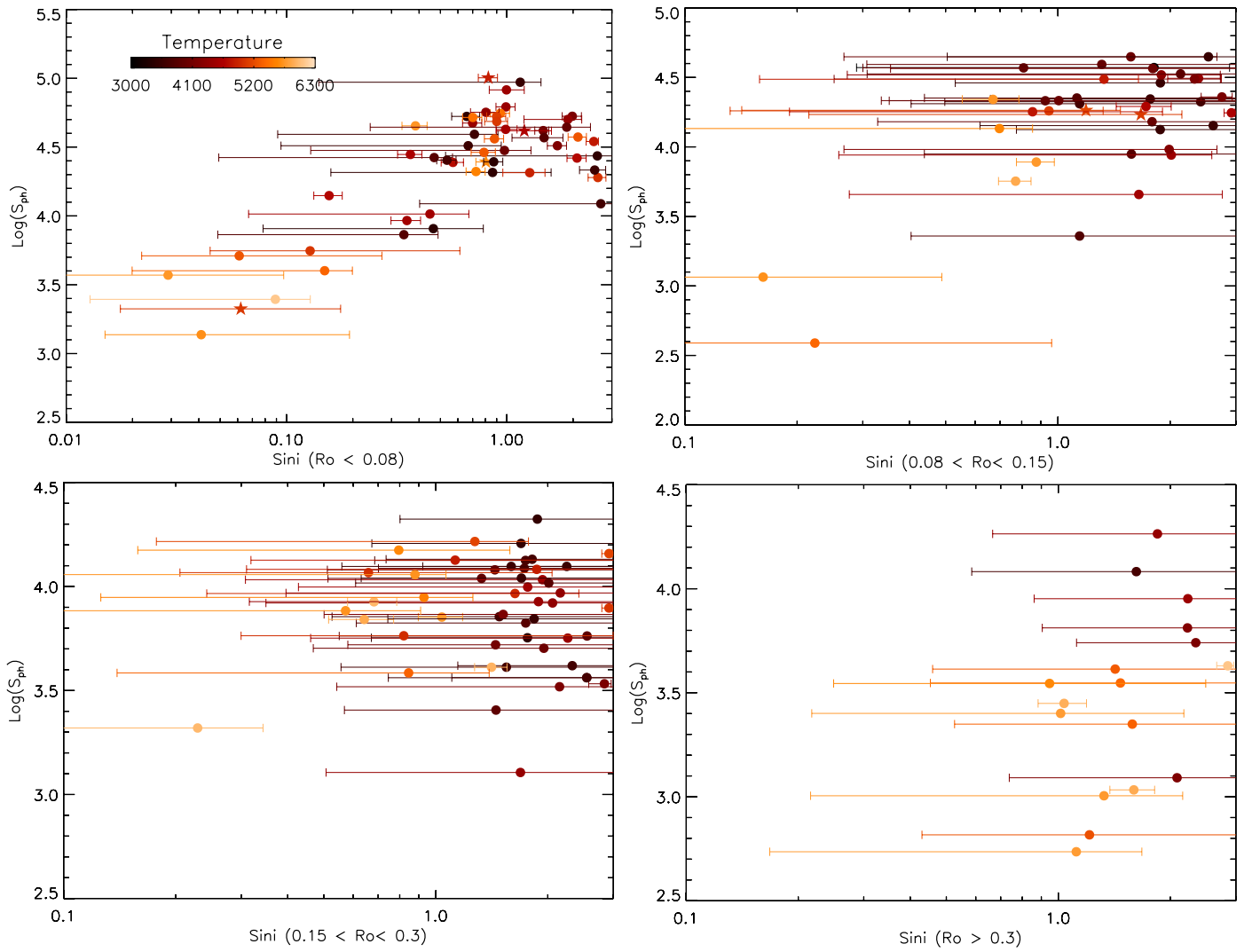


**Fig. 8.** The amplitude of lightcurve modulation  $S_{ph}$  (McQuillan et al. 2014) vs. inclination for different range of Rossby number.

lines (Unruh & Collier Cameron 1995), the uncertainty of  $v \sin i$  (Berdyugina 1998), or the differential rotation (Hackman et al. 2001), although these factors are not a general explanation for all the polar cap. Moreover, the capacity of Doppler imaging to recover features near the equator is seriously weakened because of the less differential rotation, reduced area and contrast (Berdyugina 1998, 2005; Rice 2002). Features near the equator are smeared and only the strongest features can be recovered (Rice et al. 1989; Rice 2002). Those disadvantages of Doppler imaging indicate that our result of LDAR near the equator could be more reliable. Another potential explanation for the contradiction is that polar spots are more stable (or difficult to erupt), so that flares of polar cap are rare. This explanation may be supported by Younes et al. (2020), which finds that a flare of the polar cap was triggered by the global dipolar pattern implying that it is difficult to erupt. However, we suggest that, to settle the contradiction, further studies on flares of those famous polar-cap stars can provide critical information.

The previous study on fast rotating M dwarfs found that their magnetic field geometries had two states: dipole and multipole (Gastine et al. 2013; Kochukhov 2021). The magnetic field strength of the multipole state saturates at about 4 kG, while that of the dipole state could exceed 4 kG and does not exhibit a saturation (Shulyak et al. 2017). The difference of the magnetic

field strength of the two states was also revealed by the activity proxy of X-ray luminosity (Shulyak et al. 2017). M dwarfs with dipole state may account for their higher activity level as shown in Figure 6. However, the different activity levels of the two states make it difficult to determine the relationship between the activity and inclination for M-type stars. Nevertheless, given that M dwarfs with the dipole state are associated with the polar cap (Morin et al. 2010) and that giant flares have been found at high latitudes of fully convective stars (Ilin et al. 2021), we suggest that M-type stars may have different LDAR with the Sun.

The uncertainty of the inclination of M-type stars increases rapidly as  $v \sin i$  declines with decreasing stellar mass. Their low luminosity is also unfavorable to be observed with high-resolution spectroscopy and high-precision photometry. To verify the relationship between the flaring activity and inclination for M dwarfs, more high-precision observations are required.

### 3.3. Can the LDAR be revealed by other proxies?

The flaring activity is probably the unique proxy that can reveal LDAR of stars under the current conditions of observation because: i) It only reflects the contribution from active regions. The chromospheric activity  $R'_{HK}$  and coronal activity  $R_X$  include the contribution from the whole stellar hemisphere (Regardless

of whether there is an active region or not, a local stellar region will have a contribution to the activity proxy  $R'_{\text{HK}}$  and  $R_X$ ). This may greatly dilute the contribution of active regions, resulting in that the variation of those proxies is small. For example, the variation of  $R'_{\text{HK}}$  between the maximum and minimum of a solar cycle is  $\sim 18\%$  (Egeland et al. 2017), while the variation of flaring activity is at least 360% (Figure 4). We have investigated the relation between  $R'_{\text{HK}}$  and inclination and did not find any solid relation. ii) The observation of a flare is independent of the inclination. For example, the proxy of lightcurve modulation (McQuillan et al. 2014; Santos et al. 2021) caused by starspots only reflects the contribution from active regions. However, its amplitude  $S_{\text{ph}}$  depends on the inclination. It will be smaller if observed from pole-on and larger from equator-on (Figure 8), as the invisible region decreases. In other words, we cannot identify whether the variation of the amplitude is caused by LDAR or inclination from Figure 8. However, the top left panel of Figure 8 can validate the calculation of inclination for fast rotating stars (lower inclination should have smaller  $S_{\text{ph}}$ ) and indicates  $S_{\text{ph}}$  and the flaring activity have a strong correlation.

### 3.4. Implication to the dynamo theory

In the dynamo simulation of the Sun, the most important feature that needs to be reproduced is that sunspots appear at low latitudes and propagate equatorward (Charbonneau 2020; Nandy & Choudhuri 2002). LDAR is a direct and strong evidence of the underlying dynamo process (Roettenbacher et al. 2016). In our sample, the similarity of LDAR between fast rotating stars and the Sun demonstrates that they may have the same dynamo process, thus providing a crucial constraint to the stellar dynamo theory and simulation.

Our results are contrary to the expectation of previous dynamo simulations (Işık et al. 2018; Zhang et al. 2024). They predict that faster rotators have higher latitudes of active regions and form an inactive gap near the equator because of the weak latitudinal shear and the low efficiency of the toroidal field generation near the equator. To settle this discrepancy, the distribution of the latitudinal differential rotation and the role of the radial shear need to be reconsidered (Nelson et al. 2013).

On a wider scope of the dynamo theory, the popular viewpoint on the stellar dynamo is that stars in the saturated and unsaturated regime have different dynamo (the convective and solar-like dynamo), which is based on the activity dependence on rotation (Noyes et al. 1984; Wright et al. 2011; Wright & Drake 2016; Barnes 2007). Our result challenges this viewpoint because the convective and solar-like dynamo give rise to similar results as found here. If this is correct, it necessitates to establish a unified solar-like dynamo that spans the whole evolutionary stage of a star.

The previous study also finds that fully convective stars have the same activity dependence on rotation with partially convective stars, indicating that they are the solar-like dynamo (Wright & Drake 2016). Since fully convective stars do not have the tachocline, it questions the canonical scenario that the tachocline is crucial for the solar dynamo in the unsaturated regime. Because our stars are in the saturated regime that are very young main sequence or pre-main sequence stars (Barnes 2007), they also do not have the tachocline probably due to that the radiative core and convective envelop have not been coupled yet (Brun & Browning 2017; Barnes 2007). Hence, our results further challenge the importance of tachocline in the solar-like dynamo, supporting the unnecessary of tachocline as proposed by recent dy-

namo simulations (Charbonneau 2020; Nelson et al. 2013; Fan & Fang 2014; Zhang & Jiang 2022).

## 4. Conclusion

In this study, we calculate the flaring activity and inclination of about 200 stars through the 4-year lightcurves of the *Kepler* Mission and the spectra of APOGEE. We also use about 40 years of solar flaring data to simulate observing the Sun through the *Kepler* Mission from equator-on to pole-on and obtained the relationship between the apparent flaring activity of the Sun and inclination. We compare the relationship with flaring stars with different inclinations and found that fast rotators ( $Ro < 0.08$ ) have similar relation with the Sun, which indicates that their LDAR are solar-like, while the relation of slow rotators ( $Ro > 0.08$ ) need to be verified in the future due to the data quality and observation limit.

Our results provide a crucial constraint to dynamo theory and its simulation, and also imply that fast rotators have the same dynamo process as the Sun, contrary to the numerical simulations. Meanwhile, it provides a strong implication on the dynamo evolution that the solar-like dynamo may be applied to the whole evolutionary stage of a star, which is also contrary to the popular viewpoint.

Moreover, our results contradict the prevailing viewpoint that polar spots are widespread in fast rotators. Although we present several potential reasons for the contradiction, we cannot obtain a solid and general explanation. We suggest that to settle this issue, further studies on flares of those famous polar-cap stars can provide critical information.

*Acknowledgements.* We sincerely thank J. Jiang, B.F. Healy, F. Spada and K. Namekata for discussion and help. Jifeng Liu acknowledges support from the New Cornerstone Science Foundation through the New Cornerstone Investigator Program and the XPLOER PRIZE. Xin Cheng and Zhanhao Zhao acknowledge support from the Strategic Priority Research Program of the Chinese Academy of Sciences, Grant No. XDB0560000. Yijun Hou acknowledges support from the National Natural Science Foundation of China (12273060), the Youth Innovation Promotion Association CAS (2023063) and the Strategic Priority Research Program of CAS (XDB0560000). ZeXi Niu acknowledges support from the National Natural Science Foundation of China through grant No. 12303039 and No. 12261141690.

## References

- Abdurro'uf, Accetta, K., Aerts, C., et al. 2022, *ApJS*, 259, 35  
 Barnes, S. A. 2007, *ApJ*, 669, 1167  
 Benomar, O., Bazot, M., Nielsen, M. B., et al. 2018, *Science*, 361, 1231  
 Berdyugina, S. V. 1998, *A&A*, 338, 97  
 Berdyugina, S. V. 2005, *Living Reviews in Solar Physics*, 2, 8  
 Boro Saikia, S., Marvin, C. J., Jeffers, S. V., et al. 2018, *A&A*, 616, A108  
 Bruls, J. H. M. J., Solanki, S. K., & Schuessler, M. 1998, *A&A*, 336, 231  
 Brun, A. S. & Browning, M. K. 2017, *Living Reviews in Solar Physics*, 14, 4  
 Charbonneau, P. 2020, *Living Reviews in Solar Physics*, 17, 4  
 Chen, Y., Girardi, L., Bressan, A., et al. 2014, *MNRAS*, 444, 2525  
 Choudhuri, A. R. 2017, *Science China Physics, Mechanics, and Astronomy*, 60, 19601  
 Choudhuri, A. R. & Gilman, P. A. 1987, *ApJ*, 316, 788  
 Claret, A. & Bloemen, S. 2011, *A&A*, 529, A75  
 Deshpande, R., Blake, C. H., Bender, C. F., et al. 2013, *AJ*, 146, 156  
 Doyle, A. P., Davies, G. R., Smalley, B., Chaplin, W. J., & Elsworth, Y. 2014, *MNRAS*, 444, 3592  
 Egeland, R., Soon, W., Baliunas, S., et al. 2017, *ApJ*, 835, 25  
 Eyer, L., Audard, M., Holl, B., et al. 2023, *A&A*, 674, A13  
 Fan, Y. & Fang, F. 2014, *ApJ*, 789, 35  
 Fang, X.-S., Zhao, G., Zhao, J.-K., Chen, Y.-Q., & Bharat Kumar, Y. 2016, *MNRAS*, 463, 2494  
 Gastine, T., Morin, J., Duarte, L., et al. 2013, *A&A*, 549, L5  
 Gastine, T., Yadav, R. K., Morin, J., Reiners, A., & Wicht, J. 2014, *MNRAS*, 438, L76

- Gilhool, S. H., Blake, C. H., Terrien, R. C., et al. 2018, *AJ*, 155, 38
- Hackman, T., Jetsu, L., & Tuominen, I. 2001, *A&A*, 374, 171
- Hathaway, D. H. 2015, *Living Reviews in Solar Physics*, 12, 4
- Healy, B. F. & McCullough, P. R. 2020, *ApJ*, 903, 99
- Healy, B. F., McCullough, P. R., Schlauffman, K. C., & Kovacs, G. 2023, *ApJ*, 944, 39
- Hirano, T., Sanchis-Ojeda, R., Takeda, Y., et al. 2014, *ApJ*, 783, 9
- Holtzman, J. A., Hasselquist, S., Shetrone, M., et al. 2018, *AJ*, 156, 125
- İşik, E., Solanki, S. K., Krivova, N. A., & Shapiro, A. I. 2018, *A&A*, 620, A177
- Ilin, E., Poppenhaeger, K., Schmidt, S. J., et al. 2021, *MNRAS*, 507, 1723
- Jackson, R. J. & Jeffries, R. D. 2010, *MNRAS*, 402, 1380
- Jackson, R. J. & Jeffries, R. D. 2014, *MNRAS*, 441, 2111
- Jaehrig, K., Somers, G., & Stassun, K. G. 2019, *ApJ*, 879, 39
- Kim, Y.-C. & Demarque, P. 1996, *ApJ*, 457, 340
- Kochukhov, O. 2021, *A&A Rev.*, 29, 1
- Kostogryz, N. M., Shapiro, A. I., Witzke, V., et al. 2024, *Nature Astronomy*
- Kretzschmar, M. 2011, *A&A*, 530, A84
- Landin, N. R., Mendes, L. T. S., & Vaz, L. P. R. 2010, *A&A*, 510, A46
- Lehtinen, J. J., Spada, F., Käpylä, M. J., Olsper, N., & Käpylä, P. J. 2020, *Nature Astronomy*, 4, 658
- Maehara, H., Shibayama, T., Notsu, Y., et al. 2015, *Earth, Planets and Space*, 67, 59
- Masuda, K. & Winn, J. N. 2020, *AJ*, 159, 81
- McQuillan, A., Mazeh, T., & Aigrain, S. 2014, *ApJS*, 211, 24
- Mittag, M., Schmitt, J. H. M. M., & Schröder, K. P. 2018, *A&A*, 618, A48
- Morin, J., Donati, J. F., Petit, P., et al. 2010, *MNRAS*, 407, 2269
- Namekata, K., Sakaue, T., Watanabe, K., et al. 2017, *ApJ*, 851, 91
- Nandy, D. & Choudhuri, A. R. 2002, *Science*, 296, 1671
- Nelson, N. J., Brown, B. P., Brun, A. S., Miesch, M. S., & Toomre, J. 2013, *ApJ*, 762, 73
- Noyes, R. W., Hartmann, L. W., Baliunas, S. L., Duncan, D. K., & Vaughan, A. H. 1984, *ApJ*, 279, 763
- Piskunov, N. E., Tuominen, I., & Vilhu, O. 1990, *A&A*, 230, 363
- Reiners, A., Basri, G., & Browning, M. 2009, *ApJ*, 692, 538
- Rice, J. B. 2002, *Astronomische Nachrichten*, 323, 220
- Rice, J. B., Wehlau, W. H., & Khokhlova, V. L. 1989, *A&A*, 208, 179
- Roettenbacher, R. M., Monnier, J. D., Korhonen, H., et al. 2016, *Nature*, 533, 217
- Santos, A. R. G., Breton, S. N., Mathur, S., & García, R. A. 2021, *ApJS*, 255, 17
- Schuessler, M. & Solanki, S. K. 1992, *A&A*, 264, L13
- Shibayama, T., Maehara, H., Notsu, S., et al. 2013, *ApJS*, 209, 5
- Shulyak, D., Reiners, A., Engeln, A., et al. 2017, *Nature Astronomy*, 1, 0184
- Simonian, G. V. A., Pinsonneault, M. H., Terndrup, D. M., & van Saders, J. L. 2020, *ApJ*, 898, 76
- Somers, G., Cao, L., & Pinsonneault, M. H. 2020, *ApJ*, 891, 29
- Somers, G. & Stassun, K. G. 2017, *AJ*, 153, 101
- Spada, F., Demarque, P., Kim, Y. C., Boyajian, T. S., & Brewer, J. M. 2017, *ApJ*, 838, 161
- Spada, F., Demarque, P., Kim, Y. C., & Sills, A. 2013, *ApJ*, 776, 87
- Strassmeier, K. G. 2002, *Astronomische Nachrichten*, 323, 309
- Tayar, J., Ceillier, T., García-Hernández, D. A., et al. 2015, *ApJ*, 807, 82
- Unruh, Y. C. & Collier Cameron, A. 1995, *MNRAS*, 273, 1
- Watanabe, K., Shimizu, T., Masuda, S., Ichimoto, K., & Ohno, M. 2013, *ApJ*, 776, 123
- Wright, N. J. & Drake, J. J. 2016, *Nature*, 535, 526
- Wright, N. J., Drake, J. J., Mamajek, E. E., & Henry, G. W. 2011, *ApJ*, 743, 48
- Yang, H. & Liu, J. 2019, *ApJS*, 241, 29
- Yang, H., Liu, J., Gao, Q., et al. 2017, *ApJ*, 849, 36
- Yang, H., Liu, J., Qiao, E., et al. 2018, *ApJ*, 859, 87
- Younes, G., Baring, M. G., Kouveliotou, C., et al. 2020, *ApJ*, 889, L27
- Zhang, Z. & Jiang, J. 2022, *ApJ*, 930, 30
- Zhang, Z., Jiang, J., & Kitchatinov, L. 2024, *A&A*, 686, A90

## Appendix A: Additional figures

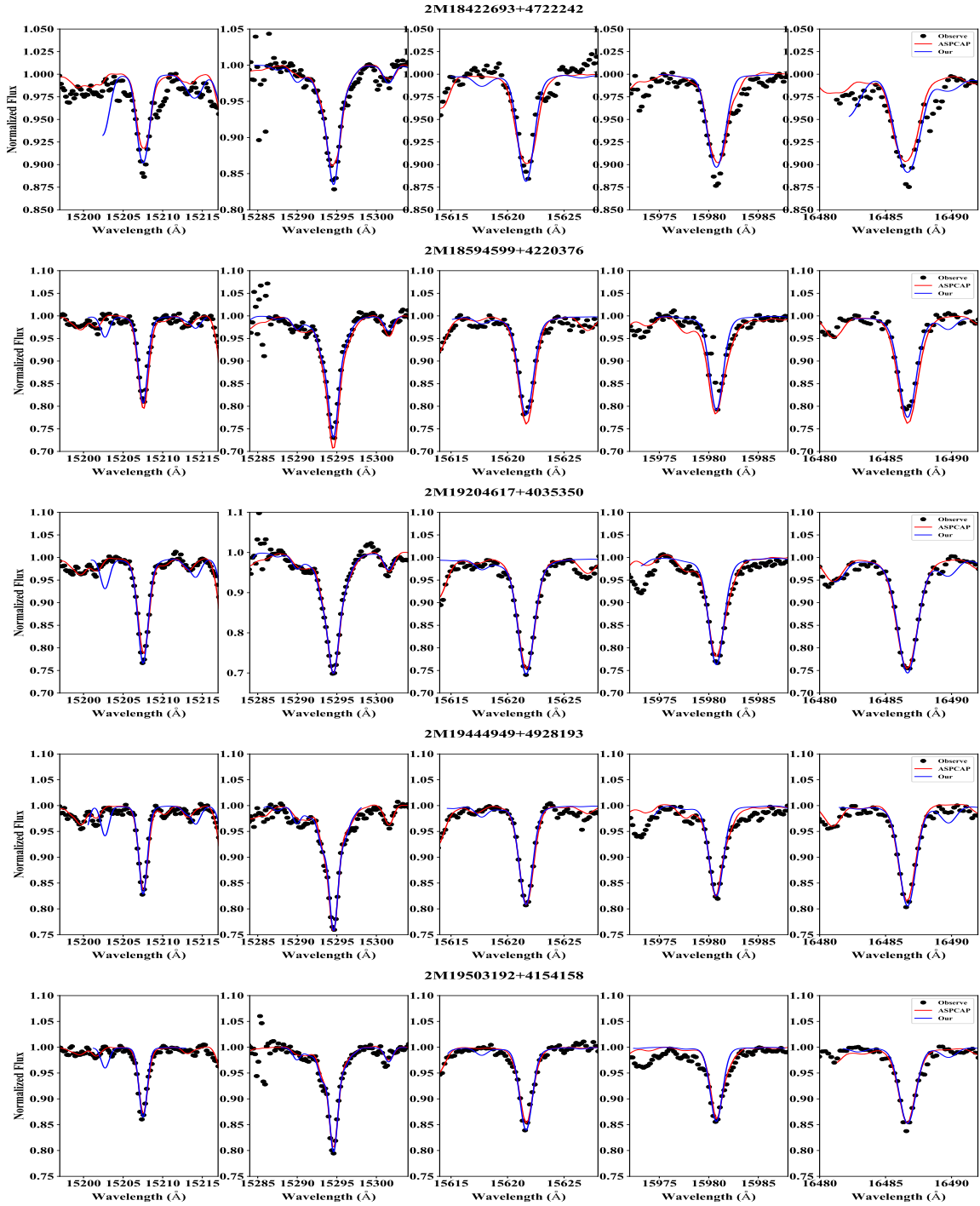


**Fig. A.1.** A comparison of the spectrum fitting between our method and that of ASPCAP. Five stars whose difference of  $v \sin i$  is larger than  $5 \text{ km s}^{-1}$  are plotted. Each row shows a star including five Fe I lines that exhibit minimal blending. Blue lines represent the our best-fit. Red lines represent the best-fit of ASPCAP.

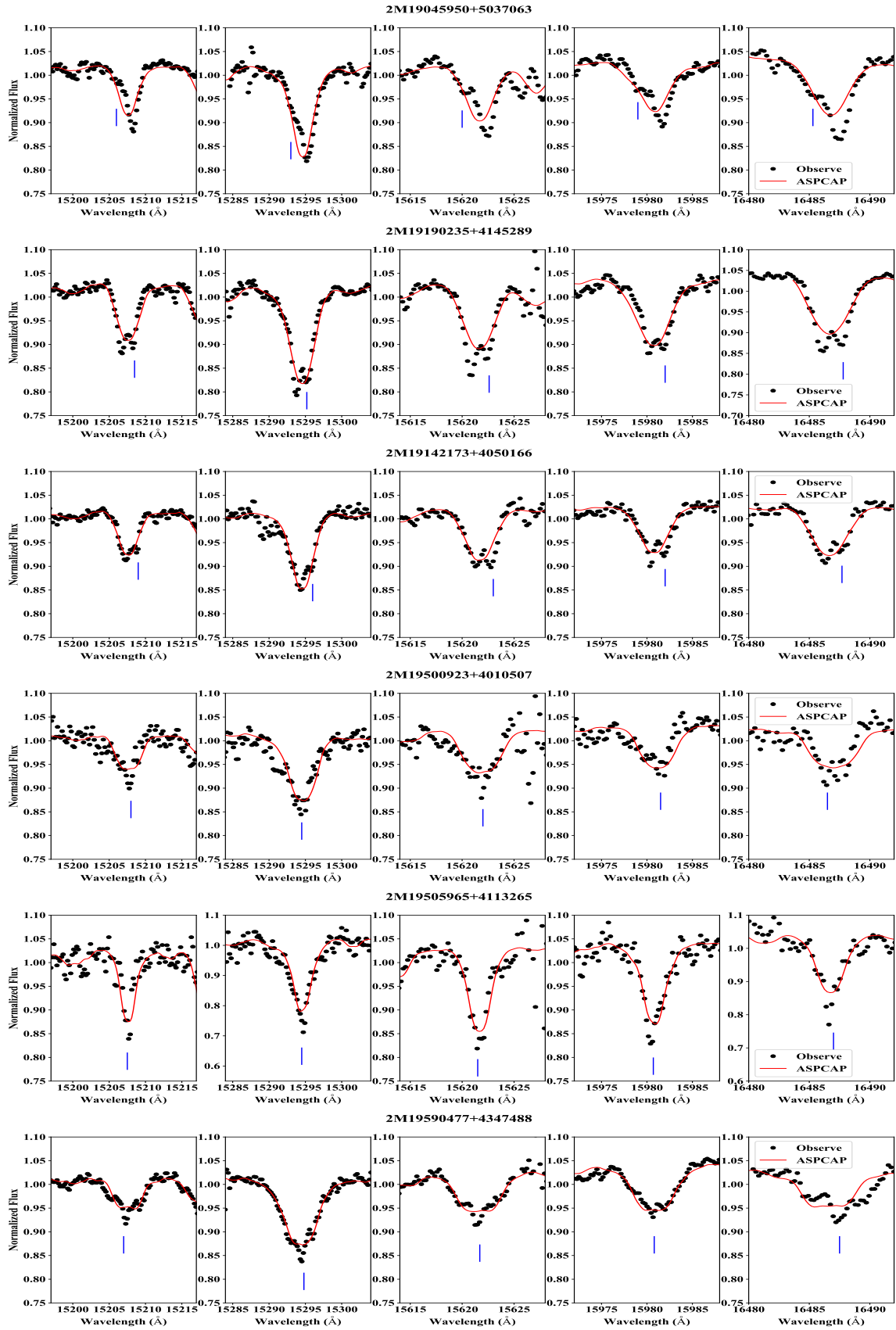


**Fig. A.2.** Illustrated examples of six visual SB2s identified in our sample. Each row shows a star including five Fe I lines that exhibit minimal blending. The vertical blue lines denote the possible companion feature. Red line represent the best-fit of ASPCAP. Those six binaries are plotted with triangle in Figure 1, but are not included in the further analysis.